Chinese Chemical Letters 33 (2022) 3641–3649

Contents lists available at ScienceDirect

Chinese Chemical Letters

journal homepage: www.elsevier.com/locate/cclet

# Crystal facet-dependent electrocatalytic performance of metallic Cu in $CO_2$ reduction reactions

Hao Zhang[a,1], Caihong He[a,1], Sumei Han[a], Zeyang Du[a], Ling Wang[a], Qinbai Yun[b], Wenbin Cao[a], Bowei Zhang[c,*], Ya-Hui Tian[d,*], Qipeng Lu[a,*]

[a] School of Materials Science and Engineering, University of Science and Technology Beijing, Beijing 100083, China
[b] Department of Chemistry, City University of Hong Kong, Hong Kong, China
[c] Institute for Advanced Materials and Technology, University of Science and Technology Beijing, Beijing 100083, China
[d] Institute of Acoustics, Chinese Academy of Sciences, Beijing 10019, China

ARTICLE INFO

*Article history:*
Received 29 September 2021
Revised 9 November 2021
Accepted 8 December 2021
Available online 11 December 2021

*Keywords:*
Copper
$CO_2$ electrochemical reduction
Crystal facet-dependence
Electrocatalysts

ABSTRACT

Developing high-performance electrocatalysts for $CO_2$ reduction reaction ($CO_2$RR) is crucial since it is beneficial for environmental protection and the resulting value-add chemical products can act as an alternative to fossil feedstocks. Nonetheless, the direct reduction of $CO_2$ into long-chain hydrocarbons and oxygenated hydrocarbons with high selectivity remains challenging. Copper (Cu) shows a distinctive advantage that it is the only pure metal catalyst for reducing $CO_2$ into multi-carbon ($C_{2+}$) products and the certain facets (*e.g.*, (100), (111), (111)) of Cu nanocrystals exhibit relatively low energy barriers for the formation of specific products (*e.g.*, CO, HCOOH, $CH_4$, $C_2H_4$, $C_2H_5OH$, and other $C_{2+}$ products). Therefore, extensive studies have been carried out to explore the relationship between the facets of Cu nanocrystals and corresponding catalytic products. In this review, we will discuss the crystal facet-dependent electrocatalytic $CO_2$RR performance in metallic Cu catalysts, meanwhile, the detailed reaction mechanisms will be systematically summarized. In addition, we will provide a personal perspective for the future research directions in this emerging field. We believe this review is helpful to guide the design of high-selectivity Cu-based electrocatalysts for $CO_2$RR.



## 1 Introduction

The rapid industrial revolution and population growth have led to a large amount of global energy consumption [1,2]. Energy heavily depends on the burning of fossil fuels, causing a significant increase of the content of $CO_2$ in atmosphere [3–5], which further results in the greenhouse effects such as melting glaciers, global warming, and gradually threatens human life [6–8]. Therefore, we are facing a crisis for excessive emission of $CO_2$. In this context, extensive studies have been carried out to control $CO_2$ emissions such as carbon capture and storage [9,10], carbon capture and utilization [11,12]. Carbon capture and storage aims to capture and store $CO_2$ in the ocean or land [13], and carbon capture and utilization intends to use $CO_2$ as feedstock for generating a variety of economically valuable products [14], including producing the food-grade $CO_2$, mineral carbonation and reduction of $CO_2$ to chemicals by catalysis. Photocatalytic and electrocatalytic $CO_2$ reduction reactions ($CO_2$RR) could convert $CO_2$ into valuable chemicals in an environmentally friendly way. Compared with photocatalytic $CO_2$RR, electrocatalytic $CO_2$RR is more efficient, which shows higher activity and selectivity for the desired products [15]. Thus, electrocatalytic $CO_2$RR becomes a hot spot in the field of energy utilization and environmental protection.

Extensive efforts have been devoted to electrocatalytic $CO_2$RR. However, it has yet to meet industrial application targets owing to technological challenges [16]. First, $CO_2$ is thermodynamically stable molecules with two C=O double bonds. A high overpotential is significantly required to achieve one-electron reduction of $CO_2$ to $CO_2^-$, ($E = -1.90$ V *vs.* standard hydrogen electrode, SHE) [17], which is the key step in the reduction process. Thus, it is necessary to input a large amount of energy to meet the requirement of thermodynamic and kinetic processes. Second, during the electrocatalysis, there is a competitive relationship between $CO_2$RR and severe side reactions (*e.g.*, hydrogen evolution reaction (HER)). When HER overpowers $CO_2$RR at the cathode side, the faradic efficiency

* Corresponding authors.
*E-mail addresses:* bwzhang@ustb.edu.cn (B. Zhang), tianyahui@mail.ioa.ac.cn (Y.-H. Tian), qipeng@ustb.edu.cn (Q. Lu).
[1] These authors contributed equally to this work.

https://doi.org/10.1016/j.cclet.2021.12.018
1001-8417/

**Table 1**
Equilibrium potentials for $CO_2$ electrolysis related reactions at pH 7 [36,37].

| Half-reactions of $CO_2$RR | $E$ (V *vs.* SHE) |
|---|---|
| $CO_2$ (g) + $2H^+ + 2e^-$ = HCOOH (l) | −0.250 |
| $CO_2$ (g) + $2H^+ + 2e^-$ = CO (g) + $H_2O$ (l) | −0.117 |
| $CO_2$ (g) + $6H^+ + 6e^-$ = $CH_3OH$ (l) + $H_2O$ (l) | 0.033 |
| $CO_2$ (g) + $8H^+ + 8e^-$ = $CH_4$ (g) + $2H_2O$ (l) | 0.173 |
| $2CO_2$ (g) + $8H^+ + 8e^-$ = $CH_3COOH$ (l) + $2H_2O$ (l) | 0.110 |
| $2CO_2$ (g) + $10H^+ + 10e^-$ = $CH_3CHO$ (l) + $3H_2O$ (l) | 0.060 |
| $2CO_2$ (g) + $12H^+ + 12e^-$ = $C_2H_4$ (g) + $4H_2O$ (l) | 0.064 |
| $2CO_2$ (g) + $12H^+ + 12e^-$ = $CH_3CH_2OH$ (l) + $3H_2O$ (l) | 0.084 |
| $2CO_2$ (g) + $14H^+ + 14e^-$ = $C_2H_6$ (g) + $4H_2O$ (l) | 0.143 |
| $3CO_2$ (g) + $18H^+ + 18e^-$ = $C_3H_7OH$ (l) + $5H_2O$ (l) | 0.103 |

(FE) of $CO_2$RR significantly decreases [18]. Furthermore, the products of $CO_2$RR are complex, including $CH_4$ [19,20], CO [21], $CH_3OH$ [22], HCOOH [23–25], $C_2H_4$ [26–29], $C_2H_6$ [30,31], $CH_3CHO$ [32], $CH_3CH_2OH$ [33], and $C_{2+}$ products [34,35]. As shown in Table 1, these products require different numbers of transferred electrons [36,37]. The complex process makes it difficult to achieve high selectivity for the desired products, especially for $C_2$ and $C_{2+}$ species. To solve the key issues above, it is urgent to develop superior catalysts to achieve desired valuable products through $CO_2$RR.

Until now, various electrocatalysts for $CO_2$RR have been studied, and two kinds of compounds are focused: Solid materials and homogeneous metal complexes [38,39]. The metallic electrocatalysts as one kind of solid materials have been applied in $CO_2$RR due to their excellent catalytic performance, facile preparation and separation after the usage [40]. According to the electrocatalytic products, single metal catalysts can be divided into four categories: (I) Metals with high selectivity to produce $H_2$ (*e.g.*, Ni, Fe, Pt and Ti), (II) metals with high selectivity to produce HCOOH (*e.g.*, Bi, Sn, Pb and In), (III) metals with high selectivity to produce CO (*e.g.*, Au, Ag, Zn and Pd) and (IV) metals with high selectivity to produce $C_2$ and $C_{2+}$ products (*e.g.*, Cu) [37,41,42]. Among the above pure metal catalysts, Cu is the only one that is capable of reducing $CO_2$ into long-chain hydrocarbons and oxygenated hydrocarbons [37]. Under certain conditions, up to 16 kinds of products can be detected on the surface of Cu catalysts during $CO_2$RR [23]. Importantly, tailoring crystal facet to optimize the catalytic activity and selectivity of Cu catalysts is a key approach to achieve high yields for multicarbon products. Meanwhile, different arrangements of atoms on the crystal facets could produce significantly diverse ratios of $C_1$, $C_2$ and $C_{2+}$ products [43]. However, up to now, there are rare reviews focusing on explaining the crystal facet-dependent selectivity and activity in Cu-based catalysts, understanding the elementary steps of reactions, revealing the corresponding $CO_2$RR process and establishing relationship between structure and performance [44].

In this review, we will comprehensively introduce the recent developments of metallic Cu catalysts with different crystal facets in $CO_2$RR, and systematically summarize the detailed reaction mechanisms for different valuable products. In addition, we will give some perspectives on the challenges and promising directions in this research field.

## 2. Reaction mechanisms of metallic Cu with different facets in CO2RR

Metallic Cu possesses thermodynamically stable face center cubic (*fcc*) crystal phase. Similar to other metals with *fcc* phase, *e.g.*, Au, Ag, Pd, Pt, the synthetic strategies for exposed facet control in Cu have been well-developed [45–48]. Through thermodynamic and kinetic controls, Cu nanocrystals with controllable exposed facets and various morphologies could be prepared, such as

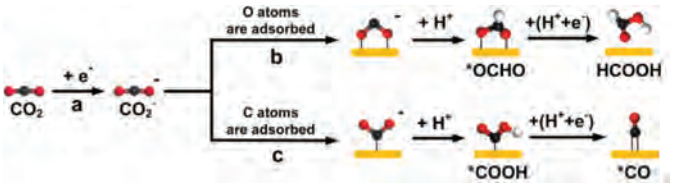


**Fig. 1.** Possible initial reaction steps of $CO_2$RR. The red, black, and white balls represent the O atom, C atom and H atom, respectively.

nanoparticles (NPs) [49,50], nanowires (NWs) [51–55], polyhedrons exposing desired crystal facets and so on.

Among the numerous synthetic strategies, wet-chemical method is considered as a commonly used approach [56–62]. In this method, capping agents are usually adopted for shape control, because they can adsorb on specific facets to change the surface free energy and tune the growth rate. As a result, the most favorable thermodynamic facets will be exposed [33,63-69]. Besides, etching agents are often employed for the construction of the exposed facets. It is reported that crystal etching can act as the reverse process of crystal growth to endow nanocrystal with high-energy facets [58]. In addition, the gas-phase-reduction method and electrochemical method have also been reported to synthesize Cu nanocrystals with various shapes (*e.g.*, cube, octahedron and dodecahedron) [70–72]. Compared with wet-chemical method, they can avoid the use of surfactants, thus facilitating the subsequent charge transfer in the electrocatalytic performance test [73].

This review does not discuss the detailed descriptions about the synthesis of metallic Cu nanostructures with different exposed facets by using these methods, since they have been reviewed previously [45–48]. Herein, we summarize the established synthetic procedures and corresponding obtained metallic Cu nanostructures with different morphologies and list them in Table 2. In the following sections, we focus on the mechanisms of crystal facet-dependent electrocatalytic performance of metallic Cu catalysts in $CO_2$RR processes.

### 2.1. The initial adsorption modes of $CO_2$ on Cu catalysts

In the pioneering research conducted by Hori and co-workers, Cu was demonstrated to be the unique electrocatalyst that can reduce $CO_2$ into valuable products [32,41,74]. However, the mechanism of $CO_2$RR is still an open question, and there is no consensus even up to now. As is well known, $CO_2$ is initially adsorbed on the catalyst surface and then reduced to $CO_2^-$ by receiving one electron (Fig. 1, step a), which requires a high overpotential [17]. Peterson and co-workers first performed density functional theory (DFT) calculations to propose insights into the detailed reaction pathways of $CO_2$RR on Cu surface [75]. The results demonstrated that two different adsorption modes of $CO_2^-$ exist: (I) If oxygen atoms are adsorbed on the surface of the catalyst (Fig. 1, step b), *OCHO intermediate will be obtained after protonation of $CO_2^-$, thus generating $HCOO^-$/HCOOH; (II) if the carbon atoms are adsorbed on the surface of catalysts (Fig. 1, step c), the carboxyl *COOH intermediate will be produced followed by the formation of *CO as a very important intermediate in $CO_2$RR [76]. It is proposed that Cu has negative adsorption energy for *CO through DFT calculations, which avoids the desorption of CO and ensures its subsequent reduction to generate desirable products [77]. As discussed in the followed sections, bifurcating reaction pathways will occur on different Cu facets after intermediate *CO was formed, which is described as “facet-dependence”. Therefore, many studies have attached importance to controlling shapes and structures of

**Table 2**
Summary of established synthetic procedures for preparing Cu nanocrystals with different facets.

| Crystal facet | Synthetic method | Precursors | Reaction condition | Structures | Ref. |
|---|---|---|---|---|---|
| Cu (111) | Wet-chemical method | $Cu(CH_3COO)$, trioctylamine, OA | 180 °C for 1 h, 270 °C for 1 h | NPs | [49] |
| Cu (111) | Wet-chemical method | $CuCl_2$, hydrazinium hydroxide | 25 °C for 2 h | NPs | [50] |
| Cu (111) | Wet-chemical and electrochemical method | Cu mesh | Annealing Cu mesh in air, electrochemical reduction | NWs | [51] |
| Cu (111) | Wet-chemical method | $CuCl_2{\cdot}2H_2O$, $Ni(acac)_2$, OLA | 80 °C for 10 min, 185 °C for 4 h | NWs | [52] |
| Cu (111) | Wet-chemical method | $Cu(acac)_2$, $Ni(acac)_2$, OLA, $CuCl_2$ | Stirred at 80 °C, aged at 165 °C for 55 min and adding $CuCl_2$ into mixture | NWs | [55] |
| Cu (111) | Wet-chemical method | CuBr, TOP, OLA | 80 °C for 15 min, 270 °C for 3 h | Octahedron | [33] |
| Cu (111) | Wet-chemical method | CuCl, TOP, OLA | 200 °C for 2 h, 335 °C for a certain time | Octahedron | [57] |
| Cu (111) | Wet-chemical method | CuCl, TOP, OLA | 200 °C for 2 h, 335 °C for 30 min | Octahedron | [59] |
| Cu (111) | Wet-chemical method | CuCl, TOP, OLA | 200 °C for 2 h, 335 °C for 20 min | Octahedron | [60] |
| Cu (111) | Gas-phase-reduction | Octahedral $Cu_2O$, CO/Ar | Thermal reduction in CO/Ar, 275 °C for 2h | Octahedron | [70] |
| Cu (111) | Wet-chemical method | CuBr, TOP, OLA | Room-temperature for 1 h, 270 °C for 1 h | Octahedron | [63] |
| Cu (111) | Wet-chemical method | CuCl, TOP, OLA | 200 °C for 2 h, 335 °C for 20 min | Octahedron | [64] |
| Cu (100) | Wet-chemical method | $CuCl_2$, HDA, glucose | Room temperature overnight, 120 °C for 3 h | NWs | [53] |
| Cu (100) | Wet-chemical method | $CuCl_2$, $NaHCO_3$, AA, CTAC | Room temperature for 4 h, 30 °C for 6 h | NWs | [54] |
| Cu (100) | Wet-chemical method | $CuCl_2{\cdot}2H_2O$, glucose, HDA | Room temperature overnight, 100 °C for 6 h | Pentagonal NWs tadpole-like NWs pentagonal bipyramid | [62] |
| Cu (100) | Electrochemical method | $CuSO_4$, sodium citrate, AA | Electrochemical reduction of $Cu_2O$ NCs | Cube | [73] |
| Cu (100) | Wet-chemical method | CuBr, TOPO, OLA | 80 °C for 15 min, 230 °C for 3 h | Cube | [33] |
| Cu (100) | Electrochemical method | $CuSO_4{\cdot}5H_2O$, KCl | Oxidative-reductive cycles | Cube | [72] |
| Cu (100) | Wet-chemical method | CuBr, TOPO, OLA | 80 °C for 15 min, 260 °C for 1 h | Cube | [59] |
| Cu (100) | Wet-chemical method | CuBr, TOPO, OLA | 80 °C for 15 min, 230 °C for 1 h | Cube | [65] |
| Cu (100) | Wet-chemical method | CuBr, TOPO, OLA | 80 °C for 15 min, 200 °C for 1 h | Cube | [66] |
| Cu (100) | Electrochemical method | CuCl, KCl | Successive oxidative-reductive cycles | Cube | [71] |
| Cu (100) | Gas-phase-reduction | Cubic $Cu_2O$, CO/Ar | Thermal reduction in CO/Ar, 275 °C for 2 h | Cube | [70] |
| Cu (100) | Wet-chemical method | CuBr, TOPO, OLA | 260 °C for 2 h | Cube | [67] |
| Cu (100) | Wet-chemical method | $CuCl_2$, DBS, hydrazine | 100 °C for 20 min | Cube | [68] |
| Cu (100) | Wet-chemical method | $Cu(acac)_2$, 1,2-hexadecanediol, octyl ether, OLA | 210 °C for 30 min | Cube | [69] |
| Cu (110) | Wet-chemical method | $Cu(CH_3COO)$, trioctylamine, OA | 180 °C for 1 h, 270 °C for 1 h | NPs | [49] |
| Cu (110) | Gas-phase-reduction | Dodecahedral $Cu_2O$, CO/Ar | Thermal reduction in CO/Ar, 275 °C for 2 h | Dodecahedron | [70] |
| Cu (110) | Wet-chemical method | CuBr, TOP, OLA | 80 °C for 15 min, 270 °C for 3 h | Dodecahedron | [33] |
| Cu (110) | Wet-chemical method | Cu NCs, TOP, Se | 60 °C for 4 h | Dodecahedron | [58] |

*OA: oleic acid, OLA: oleylamine, TOP: tri-*n*-phosphine, HDA: hexadecylamine, AA: ascorbic acid, CTAC: cetyltrimethylammonium chloride, TOPO: tri-*n*-octylphosphine oxide, DBS: dodecyl benzene sulfonic acid sodium.

**Table 3**
Summarization of preferable product on the different Cu crystal facets in $CO_2$RR.

| Catalyst | Crystal facet | Electrolyte | Major product | Potential (V) *vs.* RHE | FEs (%) | Ref. |
|---|---|---|---|---|---|---|
| Octahedron- Cu | Cu (111) | 0.1 mol/L $KHCO_3$ | $CH_4$ | −1.22 | ≈23 | [33] |
| $Cu_2O$-derived Cu | Cu (111) | 0.1 mol/L $KHCO_3$ | $CH_4$ | −1.15 | 43.5 | [19] |
| Cu single crystal | Cu (111) | 0.1 mol/L $KClO_4$ | $CH_4$ | −1.38 | 45.3 | [20] |
| $O_h$-NCs-75 nm | Cu (111) | 0.1 mol/L $KHCO_3$ | $CH_4$ | −1.25 | 55.0 | [57] |
| $Cu_{oh}$ nanocrystal | Cu (111) | 1 mol/L KOH | $CH_4$ | −0.91 | 53.0 | [59] |
| Cu NCs-320 nm/Cu | Cu (100) | 0.1 mol/L $KHCO_3$ | $C_2H_4$ | −1.05 | ≈20.0 | [72] |
| Cu NCs | Cu (100) | 0.1 mol/L $KHCO_3$ | $C_2H_4$ | −1.20 | ≈35.0 | [33] |
| $Cu_2O$-derived Cu | Cu (100) | 0.1 mol/L $KHCO_3$ | $C_2H_4$ | −1.00 | 30.6 | [19] |
| Cu NCs-44 nm | Cu (100) | 0.1 mol/L $KHCO_3$ | $C_2H_4$ | −1.10 | 41.0 | [26] |
| Cu single crystal | Cu (100) | 0.1 mol/L $KHCO_3$ | $C_2H_4$ | −1.00 | 40.4 | [32] |
| $Cu_{cub}$ nanocrystal | Cu (100) | 1 mol/L KOH | $C_2H_4$ | −0.65 | 57.0 | [59] |
| Cu NCs-70 nm | Cu (100) | 1 mol/L KOH | $C_2H_4$ | −0.8 | 51.0 | [67] |
| Cu single crystal | Cu (100) | 0.1 mol/L KI | $C_2H_4$ | −1.23 | 50.3 | [20] |
| Cu (100)@$Cu_2O$ | Cu (100) | 0.1 mol/L NaOH | $C_2H_4$ | −1.00 | 45.0 | [27] |
| Cu single crystal | Cu (110) | 0.1 mol/L $KHCO_3$ | $CH_3CHOCH_3CH_2OHCH_3COOH$ | −1.18 | 51.2 | [32] |
| Hexahedron -Cu | Cu (110) | 0.1 mol/L $KHCO_3$ | $CH_3CH_2OH$ | −1.20 | ≈25.0 | [33] |
| Cu NWs | Cu (511) | 0.1 mol/L $KHCO_3$ | $C_2H_4$ | −1.01 | 77.4 | [28] |
| Cu thin films | Cu (751) | 0.1 mol/L $KHCO_3$ | $C_2H_4$ | −0.97 | ≈28.5 | [29] |
| Cu Foils | Cu (311) | 0.1 mol/L $KHCO_3$ | HCOOH | −0.95 | ≈40.0 | [25] |

Cu nanocrystals with specific exposed facets, including (111), (100) and (110), to obtain desired products in $CO_2$RR [33,67,78,79].

### 2.2. Reaction mechanisms on Cu (111) facet

Previous research demonstrated that $CH_4$ is the main product on Cu (111) facet through a series of proton-electron transfers at near neutral pH (Table 3). Unavoidably, other byproducts could be obtained simultaneously as well [37,74,80-84].

It is controversial that whether the *CO intermediate is initially reduced to a formyl *CHO by forming a C−H bond or a *COH intermediate *via* forming an O−H bond. One viewpoint holds that $CH_4$ is derived from *CHO. Zhao and co-workers used the climbing image nudged elastic band method to calculate the saddle points and minimum energy paths (MEPs) of *CO protonation into *CHO and *COH intermediates on Cu (111) (Fig. 2a). The results suggested that the formation barriers of *CHO and *COH from *CO on Cu (111) are 0.85 and 1.39 eV, respectively [85]. Thus, the formation of *CHO is more thermodynamically favorable. Moreover, Peterson and co-workers found that *CHO can be obtained much easier than *COH on Cu (111) based on DFT calculation, and regard the protonation of *CO to *CHO as the rate-determining step (RDS) (Fig. 2b) [75], which is consistent with the conclusions of Nørskov and co-workers [75,86-88]. In addition, they summarized that formaldehyde $^*CH_2O$ and methoxy $^*CH_3O$ are intermediates for $CH_4$ production, and proposed the overall pathway proceeding as $^*CO \rightarrow {}^*CHO \rightarrow {}^*CH_2O \rightarrow {}^*CH_3O \rightarrow {}^*CH_4 + {}^*O \rightarrow CH_4 + {}^*OH \rightarrow CH_4 + H_2O$, which is indicated in Fig. 2c1.

However, some research proposed a different conclusion that $CH_4$ is originated from *COH since the *COH is more favorable to be produced *via* the proton-electron transfer [89,90]. As shown in the H-shuttling model on the Cu (111) facet (Fig. 2d), the distance between the hydrated proton and the oxygen atom of *CO became shorter from the initial, transition to final states in the formation of *COH. By using DFT to calculate the free energies for several reaction paths of $CO_2$RR on Cu (111) facet, Nie and co-workers found that the activation barriers for *CHO and *COH formation derived from *CO is 0.39 and 0.21 eV at −1.15 V (*vs.* RHE), respectively [82,83]. As a result, *COH was the key intermediate for the formation of $CH_4$ on Cu (111). As shown in Fig. 2c2, the other pathway was proposed: $^*CO \rightarrow {}^*COH \rightarrow {}^*C \rightarrow {}^*CH \rightarrow {}^*CH_2 \rightarrow {}^*CH_3 \rightarrow CH_4$. Meanwhile, they also pointed out that the pathway in Fig. 2c1 is thermodynamically unfavorable. According to the relative free energy diagram for reaction as shown in Fig. 2e, $^*CH_3O$ tends to produce $CH_3OH$ rather than $CH_4$ because the barrier for hydrogenation of oxygen atom is smaller than that of carbon atom. Additionally, Additionally, Buonsanti and co-workers synthesized octahedral Cu nanocrystals ($O_h$-NCs) with different sizes (*i.e.*, 75 nm, 150 nm and 310 nm, Fig. 2f), and further investigated their electrochemical properties [57]. The results indicated that $CH_4$ is the favored product for all samples, and the $O_h$-NCs with 75 nm achieved the best performance with 77% FEs towards $CO_2$RR and 55% FEs for $CH_4$ at −1.25 V (Fig. 2g). Because the Cu atoms at corner and edge with low coordination number (CN) are active sites for $CO_2$RR. Therefore, the smaller Cu $O_h$-NCs with highly exposed active sites exhibited the best catalytic performance. Moreover, $CH_3OH$ was demonstrated to be the byproduct on Cu (111) in $CO_2$RR [75]. Therefore, it can be confirmed that Cu (111) tends to generate $CH_4$ through *COH as the intermediate.

In addition, the product distribution on Cu (111) in $CO_2$RR is determined by electrocatalytic reaction conditions [84,91-95]. By taking the kinetic barrier and solvent effect into account, first quantum mechanics (QM) study showed that the $C_1$ and $C_2$ pathways on Cu (111) are competitive and the final products vary with the pH value [96]. As shown in Fig. 3, at low pH, $C_2$ pathways are kinetically unfavorable while $C_1$ pathways are promoted *via* *COH intermediate to form $CH_4$. At neutral pH, the $C_1$ and $C_2$ pathways share the common intermediate, *i.e.*, *COH, and the multi-carbon products formed by CO−COH coupling [80]. At high pH, the coverage of *H decreases, which leads to a possibly larger portion of *CO on the surface. $C_1$ pathway is suppressed, and C−C coupling through *CO dimerization increases. Huang and co-workers demonstrated that the high coverage of *CO favors the *CO dimerization on Cu (111) [19]. The *CO coverage from 5/18 to 10/18 monolayer (ML) resulted in a decreased energy barrier around 0.5 eV, which is caused by the weakening of the Cu−*CO bond at higher *CO coverage. Besides, the FEs of $C_2H_4$ could achieve 30.6% when the applied potential was −1.0 V (*vs.* RHE). Additionally, in $CO_2$RR, graphitic carbon species (Cu=$^*CH_2$) have been detected by X-ray photoelectron spectroscopy and Auger electron spectroscopy measurement. Besides, $^*CH_2$ was regarded as the precursor of $C_2H_4$ [97]. Therefore, it is not surprising to find the generation of a bit $C_2H_4$ as byproduct on Cu (111) during the formation of $CH_4$.

### 2.3. Reaction mechanisms on Cu (100) facet

The $CO_2$RR processes and corresponding mechanisms on Cu (100) are more complicated compared with those on Cu (111). The

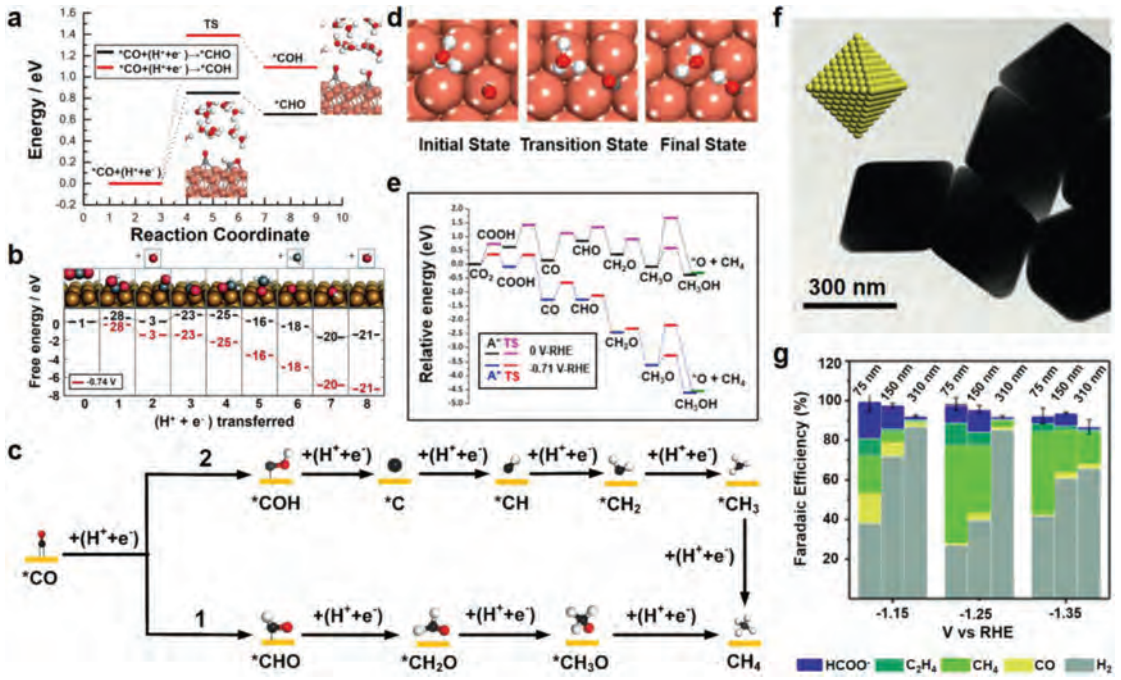


**Fig. 2.** (a) The MEP analysis of *CO reduction into *CHO and *COH intermediates on Cu (111). Reproduced with permission [85]. Copyright 2019, American Chemical Society. (b) Free energy diagrams for the lowest energy pathways to $CH_4$. Reproduced with permission [75]. Copyright 2010, Royal Society of Chemistry. (c) Possible pathways for $CH_4$ on Cu (111). The red, black, and white balls represent the O atom, C atom and H atom, respectively. (d) Optimized structures of different states involved in *CO reduction to *COH in the H-shuttling model on the Cu (111) facet. Reproduced with permission [90]. Copyright 2016, American Chemical Society. (e) Relative free energy diagrams of pathway through a *CHO intermediate. Reproduced with permission [82]. Copyright 2014, Elsevier. (f) TEM image of the octahedral Cu nanocrystals. (g) FEs of the three sizes of Cu $O_h$-NCs. Reproduced with permission [57]. Copyright 2019, Royal Society of Chemistry.

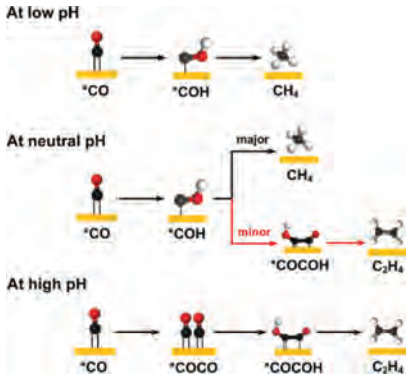


**Fig. 3.** The pH-dependent mechanism of $CO_2$RR on Cu (111). The red, black, and white balls represent the O atom, C atom and H atom, respectively.

detailed experimental analyses combined with the DFT calculations have been carried out in the published literatures. Herein, we list the overall roadmap of $CO_2$RR on Cu (100) based on the revealed mechanisms in Figs. 4a, b and d.

Currently, Cu (100) is regarded as the suitable facet for the formation of $C_2H_4$ [86,98]. Three pathways to C−C coupling formation on Cu (100) have been summarized: (I) $*CO + *CHO \rightarrow *COCHO$, (II) $*CO + *COH \rightarrow *COCOH$, (III) $*CO + *CO \rightarrow *COCO$. These pathways are considered to be related with the applied potential ($U$). Head-Gordon and co-workers have developed a micro-kinetic model to predict the Gibbs free energy of elementary steps involved in $CO_2$RR [99]. They deemed that C−C bond formation proceeds *via* *CO dimerization at low overpotential, while *via* the combination of *CO and *CHO at high overpotentials. By employing the ab initio molecular metadynamics simulations, Goddard and co-workers proposed a reaction mechanism of $C_2H_4$ for all potentials [100]. When $U < -0.8$ V (*vs.* RHE), *CHO formation is through protonation of *CO, furthermore, the obtained *CHO tends to react with *CO to generate *COCHO as an initial intermediate. As Fig. 4a shows, a more concrete pathway is proposed: $*COCHO \rightarrow *CHOCHO \rightarrow *CHOCH_2O \rightarrow *CHOCH_2OH \rightarrow *CH_2CHO \rightarrow C_2H_4$ [76]. When $U > -0.6$ V (*vs.* RHE), the RDS, *i.e.*, the formation of *COCO dimer through the coupling of *CO intermediate, leads to a pH-independent $C_2H_4$ production [43,81,101,102]. By calculating the free-energy barrier for the transition state saddle point ($\Delta G^{\ddagger}$), the explicit explanation is offered: *COCO dimer is first hydrated to *COCOH followed by the generation of *COHCOH instead of *CCO. The $\Delta G^{\ddagger}$ for the formation of *COHCOH is 0.67 eV, lower than that of *CCO, which makes it thermodynamically favorable [100]. As shown in Fig. 4b, the pathway was raised: $*CO + *CO \rightarrow *COCO \rightarrow *COCOH \rightarrow *COHCOH \rightarrow *C{=}COH \rightarrow *CH{=}COH \rightarrow *CH{=}C \rightarrow *CH{=}CH \rightarrow *CH_2{=}CH \rightarrow C_2H_4$. This mechanism can give a proper explanation for the experimental observation that Cu (100) possess a high activity for C−C coupling at low overpotentials. Through successive oxidative-reductive cycles, Nilsson and co-workers transformed the starting polycrystalline Cu into the Cu cubic nanostructure, which means that the (100) facets are exposed (Fig. 4c) [71]. The obtained $CO_2$RR performance indicated that Cu (100) favors the C−C coupling with the highest selectivity for $C_2H_4$ formation at the lowest onset potential (−0.6 V *vs.* RHE) compared with other Cu surfaces. However, by using the computational hydrogen electrode (CHE) model [103], Calle-Vallejo and co-workers proposed another mechanism to explain the reaction processes on Cu (100) at low overpotential [104,105]. They agreed with the initial reaction steps ($*CO + *CO \rightarrow *COCO \rightarrow *COCOH$) but proposed different views on the follow-up steps. They illustrated that *COCOH tended to form *CCO and projected the pathway: $*CO + *CO \rightarrow *COCO \rightarrow *COCOH \rightarrow *CCO \rightarrow *CHCO \rightarrow *CHCHO \rightarrow *CH_2CHO \rightarrow C_2H_4 + H_2O$ (Fig. 4d). It is also reported that *CO dimerization process is geometry-sensitive and shows a preference

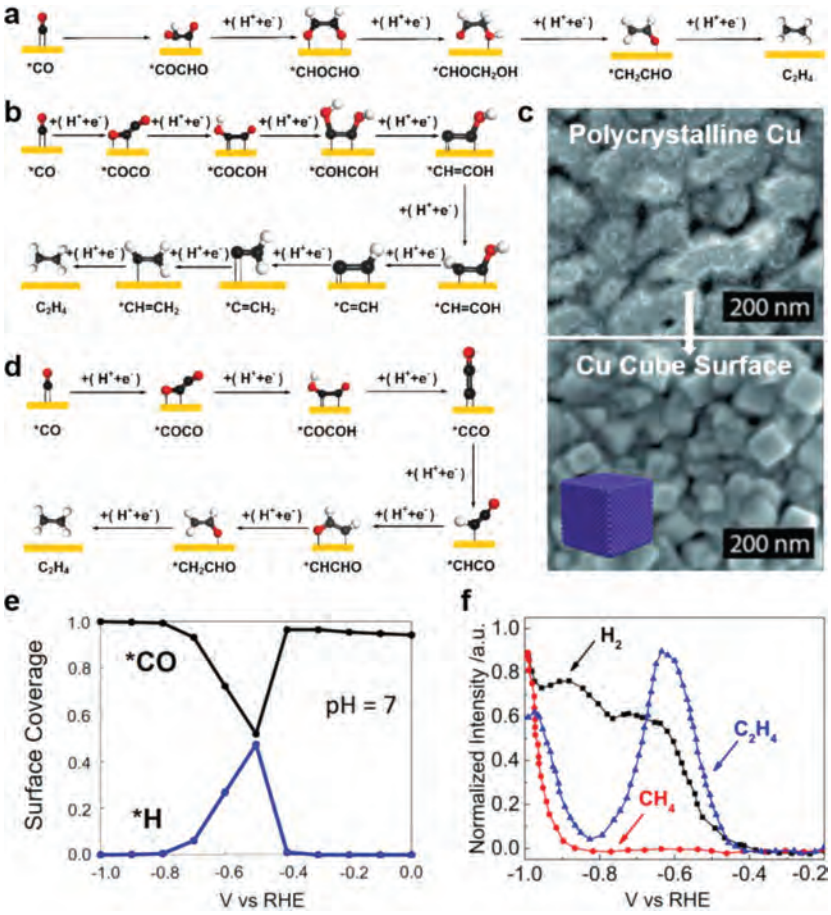


**Fig. 4.** (a) Possible pathways of $CO_2$RR on Cu (100) at high potential. (b) Possible pathways of $CO_2$RR on Cu (100) at low potential. (c) SEM images of the change process from polycrystalline Cu to the Cu Cube surface. Reproduced with permission [71]. Copyright 2015, Wiley-VCH. (d) The other possible pathway of $CO_2$RR on Cu (100) at low potential. (e) Diagram of the surface coverage of *CO and *H at different potential. Reproduced with permission [99]. Copyright 2016, American Chemical Society. (f) Diagram of reduction of CO to $C_2H_4$, $H_2$, and $CH_4$, determined with OLEMS. Reproduced with permission [100]. Copyright 2017, National Academy of Sciences. In (a), (b) and (d), the red, black, and white balls represent the O atom, C atom and H atom, respectively.

for the Cu (100) surface, which possesses square symmetry of atoms arrangement [106]. When $-0.8\,V < U < -0.6\,V$ (*vs.* RHE), the increase of *H binding energy leads to a higher coverage content of *H by displacing *CO on the surface sites. This conclusion is in accordance with the experimental observation (Fig. 4e) [99]. Consequently, HER is promoted with restraining the $C_2$ formation (Fig. 4f).

It is reported that there are other $C_2$ products formed on Cu (100) as well [27,107,108], because $*CH_2CHO$ intermediate will bifurcate into other pathways to produce $*CH_3CH_2OH$, $CH_3CHO$ and $CH_3COOH$ although Cu (110) is the most favorable facet for the formation of them [32,74]. The related mechanisms will be discussed in Section 2.4.

### *2.4. Reaction mechanisms on Cu (110) facet*

In the early 2000s, Hori and co-workers have demonstrated that Cu (110) favors the production of oxygenated hydrocarbon in $CO_2$RR compared with Cu (100) and Cu (111), such as $CH_3CH_2OH$, $CH_3CHO$ and $CH_3COOH$ [32,74]. But it does not mean that oxygenates are major products. Recently, it is speculated that sites of Cu (110) facet primarily produce $CH_3CHO$, followed by the further reduction to $CH_3CH_2OH$ [78]. Huang and co-workers demonstrated that $CH_3CH_2OH$ formed on Cu (110) with better selectivity and activity than those on Cu (100) and Cu (111) [19]. However, the mechanism investigations conducted on the Cu (110) surface are rare, which is primarily related to the instability of Cu (110) facet due to the surface reconstructions during the process of electrocatalysis [109].

There is certain association among the formation of $CH_3COOH$, $CH_3CHO$ and $CH_3CH_2OH$ and the current efficiency of $CH_3CHO$, $CH_3CH_2OH$ is positively correlated with that of $CH_3COOH$ (Fig. 5a) [32]. It is reported that $*CH_2CHO$ is the commonly shared intermediate of them. As Fig. 5b shows, $*CH_2CHO$ is first hydrogenated to vinyl alcohol $*CH_2CHOH$ [76]. After the rearrangement of $*CH_2CHOH$, the $CH_3CHO$ can be obtained since $*CH_2CHOH$ is the tautomer of $CH_3CHO$. Meanwhile, $CH_3CH_2OH$ can be obtained through consecutive protonation of $*CH_2CHOH$. Chen and co-workers prepared the hexarhombic docadehedron-like (H–Cu), cube-like, octahedron-like Cu nanoscale single crystals [33]. The morphology of H–Cu is shown in Fig. 5c, H–Cu possesses the most edges among the three samples based on the geometry. Furthermore, it is well known that the atomic arrangement along the edge side can be regarded as the (110) facet. They used H–Cu as the electrocatalyst for $CO_2$RR and performed theoretical calculation to compute the formation energy of key steps. The results indicated that Cu (110) favored a route to $CH_3CHO$, because the formation energy of $CH_3CHO$ was lower than that of adsorbed *O and $C_2H_4$ (Fig. 5d). Moreover, they thought that $CH_3CHO$ would further be reduced to $CH_3CH_2OH$, and as can be seen in Fig. 5e, the H–Cu could reduce $CO_2$ to $CH_3CH_2OH$ with FEs $\approx$ 25% at $-1.2$ V and with FEs $>$ 10% from $-1.15$ V to $-1.25$ V.

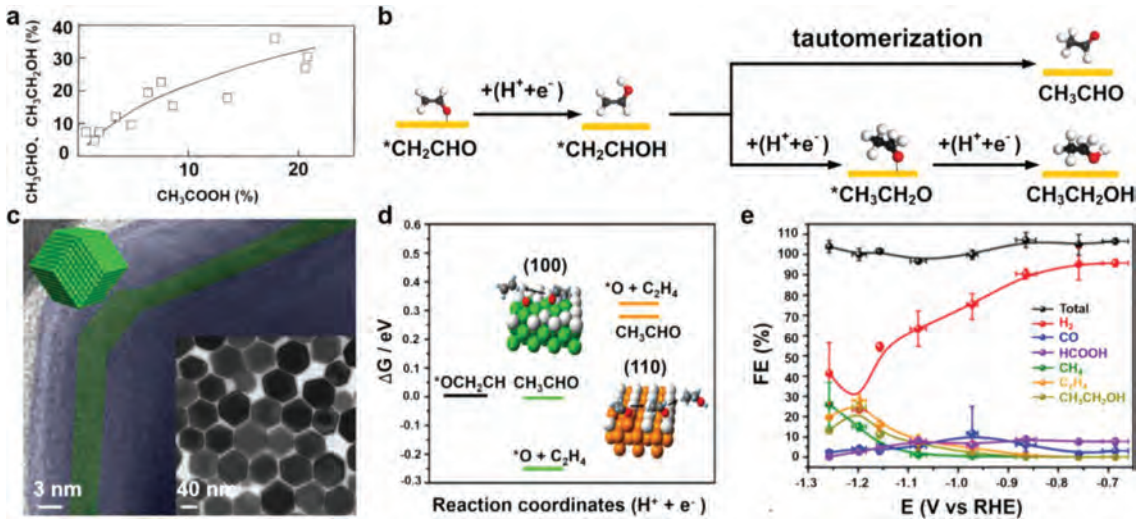


**Fig. 5.** (a) Correlation of the sum of the current efficiency of $CH_3CHO$ and $C_2H_5OH$ with that of $CH_3COOH$. Reproduced with permission [32]. Copyright 2003, Elsevier. (b) Possible mechanistic pathways of $CO_2RR$ on Cu (110). The red, black, and white balls represent the O atom, C atom and H atom, respectively. (c) HR-TEM image of rhombic dodecahedron-like Cu nanocrystal. The insight is the TEM image. (d) Calculated formation energy of $*OCH_2CH$, $*OCH_2CH_2$, $CH_3CHO$, $*O$, and $C_2H_4$ on Cu (100) and Cu (110). (e) Potential-dependent FEs curves of gas-phase products and liquid-phase products. Reproduced with permission [33]. Copyright 2019, American Chemical Society.

As shown in Table 3, $CH_3COOH$ is another product of the $CO_2RR$ on Cu (110), while the reaction mechanisms have not received much attention. Koper and co-workers suggested that, at high potentials, the local alkaline environment near the electrode can promote $CH_3CHO$ to yield $CH_3CH_2OH$ and $CH_3COO^-$ *via* a Cannizzaro-type reaction: $2CH_3CHO + OH^- \rightarrow CH_3CH_2OH + CH_3COO^-$ [110]. However, the observed ratio of these two products is not in accordance with the stoichiometric ratio. $CH_3COO^-$ is the predominant product. Furthermore, the potential required for the formation of $CH_3COO^-$ from $CH_3CHO$ (−1.5 to −2.0 V *vs.* RHE) is higher than that of $CO_2RR$ [76]. Thus, there must be additional pathways to $CH_3COO^-$ apart from the Cannizzaro mechanism. Unfortunately, to date, there have been few studies about the pathways of $CH_3COOH$ on Cu (110) facet in $CO_2RR$. Therefore, it is necessary to clarify the related mechanisms in future work.

### 2.5. Reaction mechanisms on high-index facets

High-index facets are a kind of open structures, which are denoted by a set of Miller indices (hkl) with at least an index being greater than one [29,111]. Usually, in terms of catalytic performance, metals with high-index facets are considered to be one of the best candidates for catalytic applications owing to their high density of low-coordinated atoms on step, edge, and kink sites. However, the high-index facets with high chemical reactivity always own poor stability, which are not widely accessible compared with low-index facets [112]. The reported experimental results have been listed in Table 3.

For the first time, Hori and co-workers explored the Cu electrodes with high-index facet-based electrocatalysts in $CO_2RR$ [32,74]. For example, the Cu (110) step was introduced into Cu (100) terrace and acquired electrode surface comprises *n* atomic rows of (100) terrace and one atomic height of (110) step. According to the Lang, Joyner and Somorjai notation, these surfaces can be named as Cu (*S*)-[*n*(100) × (110)] [113]. Rossmeisl and co-workers analyzed the Cu facets with respect to the CN, allowing for a unique identification of active sites (Fig. 6a) [78]. They demonstrated that the (100) × (110) step could act as the special site for $CH_3CH_2OH$ formation. With the decrease of *n* value, the step density increases, leading to the increased FEs of $CH_3CH_2OH$. As shown in Fig. 6b, Cu (310)-[3(100) × (110)] shows a higher selectivity for $CH_3CH_2OH$ compared with Cu (510)-[5(100) × (110)],

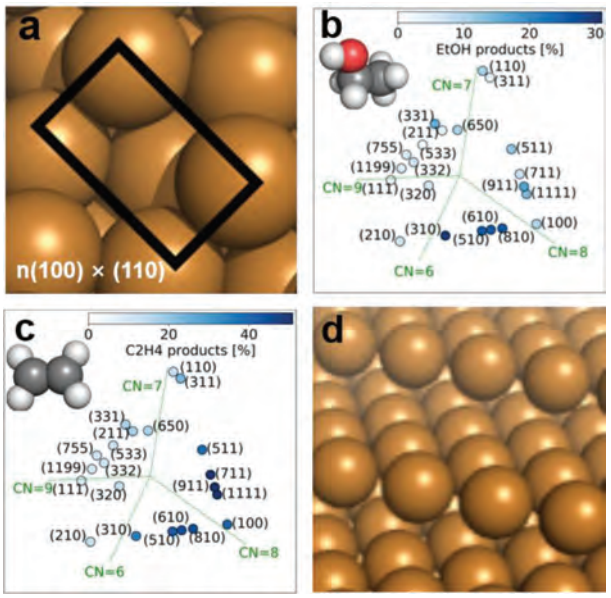


**Fig. 6.** (a) Identification of active sites of the *n*(100) × (110) step producing $CH_3CH_2OH$. (b) Selectivity of $CH_3CH_2OH$ among different Cu crystal facets. (c) Selectivity of $C_2H_4$ among different Cu crystal facets. Reproduced with permission [78]. Copyright 2019, American Chemical Society. (d) 3D atomic models of (211) facet from perspective view. Reproduced with permission [114]. Copyright 2011, Elsevier.

Cu (610)-[6(100) × (110)] and Cu (810)-[8(100) × (110)]. However, as for the Cu (210) with the high step density, the FEs of $CH_3CH_2OH$ decrease to less than 10%, which is inconsistent with the above tendency. The authors claimed that the optimal surface structure also needs a certain density of Cu (100) basal plane. Meanwhile, by incorporation of Cu (100) terrace with the Cu (111) step, another high-index facet could be created, *i.e.*, Cu (*S*)-[*n*(100) × (111)]. The results demonstrated that the surfaces containing well-ordered Cu (100) domains combined with a Cu (111) step show high selectivity for $C_2H_4$. Recently, Huang and co-workers successfully prepared the Cu NWs with Cu (511)-[3(100) × (111)] facet through *in-situ* electrochemical surface activation of pre-grown Cu NWs with (100) facets [28]. The calculation results demonstrate that the formed

step sites on Cu (511) lead to a 0.17 eV higher affinity for a single *CO adsorption compared with that of Cu (100). Moreover, Cu (511) shows a higher selectivity towards $C_2H_4$ since the free energy of two adjacent *CO adsorptions on Cu (511) is 0.44 eV lower than that on Cu (100). This result is consistent with the study of Rossmeisl's group (Fig. 6c).

The (100) step was also introduced into (111) terrace to form Cu (*S*)-[*n*(111) × (100)]. The product distribution of Cu (*S*)-[*n*(111) × (100)] resembles that of the Cu (111) single crystal. High gaseous products are detected and the yield of $C_{2+}$ products (*e.g.*, aldehydes, alcohols) is low. In this series, Cu (211)-[3(111) × (100)] has been studied extensively [75,114-118]. It contains a terrace of atoms in the (111) geometry with 3-fold coordination and a (100) step containing 4-fold coordination. The atomic models of (211) facet are shown in Fig. 6d. Remarkably, the step sites exhibit higher activity in activating bonds compared with the flat facets. Nørskov and co-workers found that Cu (211) favors the formation of $CH_4$ [117]. The DFT calculation results demonstrated that *CHO is more stable than *CO on Cu (211), resulting in the key step that protonation of *CO to *CHO being thermodynamically favorable. Besides, other series of Cu electrodes with high-index facets have been prepared as well, such as Cu (*S*)-[*n*(111) × (111)] and Cu (*S*)-[*n*(110) × (100)] [25,32].

## 3. Summary and outlook

Overall, in this review, we point out the importance of $CO_2$RR to solve the current energy crisis and environmental problems, and it is exhilarating that metallic Cu acts as a unique metal to electrochemically reduce $CO_2$ into various value-add products, including CO, HCOOH, $CH_4$, $CH_3OH$, $C_2H_4$, $C_2H_6$, $C_2H_5OH$, $CH_3CHO$, $CH_3COOH$ and other $C_{2+}$ products. Subsequently, we summarize the synthesis methods of Cu nanocrystals with different facets exposed, such as wet-chemical and electrochemical methods. Moreover, by taking the various theories into account, we discuss the reaction mechanisms of $CO_2$RR among different Cu crystal facets. It is clear that $CO_2$RR is commonly initiated by one-electron injection to the $CO_2$ reactant to form anion radical $CO_2^-$, which is adsorbed on the catalyst surface. The conversion of $CO_2^-$ to *CO or *HCOO depends on the way in which $CO_2^-$ is adsorbed on the catalysts surface. The major challenge of $CO_2$RR is to understand the bifurcating pathways from *CO to other products since *CO will be further reduced to various products on different Cu facets, which is described as "facet-dependence". Facet-dependence means that a facet exhibits a relatively lower reaction barrier for the formation of a specific product. Unfortunately, the mechanisms are still not elucidated clearly. Herein, we would like to put forward the following points to be explored in future:

(1) It is urgent to develop the operando characterization techniques to detect the intermediates and identify the active sites during the $CO_2$RR process (*e.g.*, the products protonated from *CO). Meanwhile, the theoretical calculations are important for going deep into the study of the reaction mechanisms of $CO_2$RR, such as the C−C coupling modes. These experimental results and corresponding mechanism studies are vital to set the guidelines for the rational design of the high-performance $CO_2$RR electrocatalysts.

(2) Nanocrystals with certain exposed facets are ideal materials for establishing the relationship between atomic arrangement and performance. In principle, for the prepared materials, the facet identification is the first and key step for the sequent mechanism study, especially for building correct models in DFT calculations. However, some literatures used wrong methods in facet identification, in which the observed facet based on the measured lattice fringes in TEM images are believed to be the exposed facet. For the nanocrystals with regular shapes, the exposed facet should be identified by comparing the interplanar spacings and intersection angles with the standard patterns in database. In addition, the crystalline materials with largely exposed facets often show relatively higher intensity for the corresponding diffraction peaks than that of the standard pattern in XRD characterization. This phenomenon could be used as the supplementary evidence for facet identification.

(3) Although high-index facets or metastable crystal phases exhibit higher activities, their poor stability mainly limits the further practical application. If the instability can be overcome by surface modification [119–122], it is very promising to apply high-index facet-based catalysts to $CO_2$RR.

(4) To enhance the selectivity for the desired products, other factors (*e.g.*, electrolytes [20], structure of electrodes [123], and electrolysis devices [120]) should be investigated. For example, it is reported that the activity and selectivity of $CO_2$RR is influenced by the alkali metal cation in the electrolyte. The larger cation size favors the formation of $C_2$ and $C_{2+}$ products with suppressing the HER [124]. Therefore, it is significant to regulate reaction conditions to achieve better catalytic performance.

(5) Cu-based alloy/intermetallic/composite catalysts often show much better properties for specific products in $CO_2$RR [125]. However, the related mechanisms have not been deeply studied. The synergistic effects are often mentioned in the published papers [126–128], however, the detailed mechanism studies are lacking. And how to realize the maximum utilization of the "synergistic effects" is still unclear. Thus, it is important to clarify the related mechanisms for optimizing the performance.

In the future research, more effort should be devoted to addressing these challenges. We believe that emphasizing the role of Cu facets will help to guide the designs of electrocatalysts with better performance for $CO_2$RR in the future.

## Declaration of competing interest

The authors declare that they have no known competing financial interests or personal relationships that could have appeared to influence the work reported in this paper.

## Acknowledgments

This work was financially supported by the National Natural Science Foundation of China (No. 92061119), the Beijing NOVA program (No. Z201100006820066) and the Fundamental Research Funds for the Central Universities (No. FRF-DF-20–03, No. 06500113, No. 06500119).

## References

[1] I. Dincer, M.A. Rosen, Int. J. Energy Res. 22 (1998) 1305–1321.
[2] N.S. Lewis, D.G. Nocera, Proc. Natl. Acad. Sci. U. S. A. 104 (2007) 20142-20142.
[3] C. Beer, M. Reichstein, E. Tomelleri, et al., Science 329 (2010) 834–838.
[4] M.I. Hoffert, K. Caldeira, A.K. Jain, et al., Nature 395 (1998) 881–884.
[5] A. Goeppert, M. Czaun, G.K.S. Prakash, et al., Energy Environ. Sci. 5 (2012) 7833–7853.
[6] Y. Ding, S. Zhang, L. Zhao, et al., Sci. Bull. 64 (2019) 245–253.
[7] J. Calleja-Agius, K. England, N. Calleja, Early Hum. Dev. 155 (2021) 105222.
[8] J. Xiong, M. Zhang, M. Lu, et al., Chin. Chem. Lett. 33 (2022) 1313–1316.
[9] S.M. Benson, F. Orr, MRS Bull. 36 (2008) 4317–4322.
[10] Z. Zhang, T. Wang, M.J. Blunt, et al., Appl. Energy 278 (2020) 115627.
[11] H.H. Khoo, J. Bu, R.L. Wong, et al., Energy Procedia 4 (2011) 2494–2501.
[12] M. Lehner, M. Ellersdorfer, R. Treimer, et al., BHM Berg- und Hüttenmännische Monatshefte 157 (2012) 63–69.
[13] M. Fawad, N.H. Mondol, Sci. Rep. 11 (2021) 5942.
[14] K.U.D. Calvinho, A.B. Laursen, K.M.K. Yap, et al., Energy Environ. Sci. 11 (2018) 2550–2559.
[15] C. Chen, J.F. Khosrowabadi Kotyk, S.W. Sheehan, Chem 4 (2018) 2571–2586.
[16] C. Hepburn, E. Adlen, J. Beddington, et al., Nature 575 (2019) 87–97.

[17] H. Dong, Y. Li, D. Jiang, J. Phys. Chem. C 122 (2018) 11392–11398.
[18] D. Gao, R.M. Arán-Ais, H.S. Jeon, et al., Nat. Catal. 2 (2019) 198–210.
[19] Y. Huang, A.D. Handoko, P. Hirunsit, et al., ACS Catal. 7 (2017) 1749–1756.
[20] Y. Huang, C.W. Ong, B.S. Yeo, ChemSusChem 11 (2018) 3299–3306.
[21] H.A. Hansen, J.B. Varley, A.A. Peterson, et al., J. Phys. Chem. Lett. 4 (2013) 388–392.
[22] S. Payra, S. Shenoy, C. Chakraborty, et al., ACS Appl. Mater. Interfaces 12 (2020) 19402–19414.
[23] K.P. Kuhl, E.R. Cave, D.N. Abram, et al., Energy Environ. Sci. 5 (2012) 7050–7059.
[24] J. Sun, W. Zheng, S. Lyu, et al., Chin. Chem. Lett. 31 (2020) 1415–1421.
[25] C. Zhu, Z. Zhang, L. Zhong, et al., Chem 7 (2021) 406–420.
[26] A. Loiudice, P. Lobaccaro, E.A. Kamali, et al., Angew. Chem. Int. Ed. 55 (2016) 5789–5792.
[27] R.M. Arán-Ais, F. Scholten, S. Kunze, et al., Nat. Energy 5 (2020) 317–325.
[28] C. Choi, S. Kwon, T. Cheng, et al., Nat. Catal. 3 (2020) 804–812.
[29] C. Hahn, T. Hatsukade, Y.G. Kim, et al., Proc. Natl. Acad. Sci. U. S. A. 114 (2017) 5918–5923.
[30] A. Dutta, M. Rahaman, N.C. Luedi, et al., ACS Catal. 6 (2016) 3804–3814.
[31] A. Vasileff, Y. Zhu, X. Zhi, et al., Angew. Chem. Int. Ed. 59 (2020) 19649–19653.
[32] Y. Hori, I. Takahashi, O. Koga, et al., J. Mol. Catal. A: Chem. 199 (2003) 39–47.
[33] N.T. Suen, Z.R. Kong, C.S. Hsu, et al., ACS Catal. 9 (2019) 5217–5222.
[34] Y. Zheng, A. Vasileff, X. Zhou, et al., J. Am. Chem. Soc. 141 (2019) 7646–7659.
[35] J. Li, F. Che, Y. Pang, et al., Nat. Commun. 9 (2018) 4614.
[36] S. Das, J. Perez-Ramirez, J. Gong, et al., Chem. Soc. Rev. 49 (2020) 2937–3004.
[37] S. Nitopi, E. Bertheussen, S.B. Scott, et al., Chem. Rev. 119 (2019) 7610–7672.
[38] N. Elgrishi, M.B. Chambers, X. Wang, et al., Chem. Soc. Rev. 46 (2017) 761–796.
[39] Z. Gao, J. Li, Z. Zhang, et al., Chin. Chem. Lett. 33 (2022) 2270–2280.
[40] W.W. Zhan, Q.L. Zhu, Q. Xu, ACS Catal. 6 (2016) 6892–6905.
[41] Y. Hori, H. Wakebe, T. Tsukamoto, et al., Electrochim. Acta 39 (1994) 1833–1839.
[42] C. He, L. Yu, N. Lu, et al., Nano Res. 13 (2020) 646–652.
[43] Y. Wang, Z. Wang, et al., Nat. Catal. 3 (2020) 98–106.
[44] G. Zhao, X. Huang, X. Wang, et al., J. Mater. Chem. A 5 (2017) 21625–21649.
[45] Z. Gu, H. Shen, L. Shang, et al., Small Methods 2 (2018) 1800121.
[46] S. Kim, J.M. Kim, J.E. Park, et al., Adv. Mater. 30 (2018) 1704528.
[47] N.A.C. Lah, S. Trigueros, Sci. Technol. Adv. Mater. 20 (2019) 225–261.
[48] H. Xie, T. Wang, J. Liang, et al., Nano Today 21 (2018) 41–54.
[49] K.P. Rice, E.J. Walker, M.P. Stoykovich, et al., J. Phys. Chem. C 115 (2011) 1793–1799.
[50] S.H. Wu, D.H. Chen, J. Colloid Interface Sci. 273 (2004) 165–169.
[51] D. Raciti, K.J. Livi, C. Wang, Nano Lett. 15 (2015) 6829–6835.
[52] J. Wang, H. Chen, Y. Zhao, et al., ACS Appl. Mater. Interfaces 12 (2020) 35211–35221.
[53] M. Luo, M. Zhou, R.R. Silva, et al., ChemNanoMat 3 (2017) 190–195.
[54] X. Liu, Y. Sui, X. Yang, et al., ACS Appl. Mater. Interfaces 8 (2016) 26886–26894.
[55] X. Wang, R. Wang, L. Shi, et al., J. Mater. Chem. C 6 (2018) 1048–1056.
[56] X. Ren, D. Chen, F. Tang, J. Phys. Chem. B 109 (2005) 15803.
[57] P. Iyengar, J. Huang, G.L. De Gregorio, et al., Chem. Comm. 55 (2019) 8796–8799.
[58] Z. Wang, G. Yang, Z. Zhang, et al., ACS Nano 10 (2016) 4559–4564.
[59] G.L. De Gregorio, T. Burdyny, A. Loiudice, et al., ACS Catal. 10 (2020) 4854–4862.
[60] S.C. Lu, M.C. Hsiao, M. Yorulmaz, et al., Chem. Mater. 27 (2015) 8185–8188.
[61] J.H. Kim, J.E. Park, M. Lin, et al., Adv. Mater. 29 (2017) 1702945.
[62] M. Jin, G. He, H. Zhang, et al., Angew. Chem. Int. Ed. 50 (2011) 10560–10564.
[63] P. Iyengar, M.J. Kolb, J.R. Pankhurst, et al., ACS Catal. 11 (2021) 4456–4463.
[64] K.T. Chen, W.C. Chang, S.C. Lu, et al., J. Nanomater. (2019) (2019) 1–7.
[65] H. Guo, Y. Chen, M.B. Cortie, et al., J. Phys. Chem. C 118 (2014) 9801–9808.
[66] L.M. Lyu, Y.C. Kao, D.A. Cullen, et al., Chem. Mater. 29 (2017) 5681–5692.
[67] Y. Wang, H. Shen, K.J.T. Livi, et al., Nano Lett. 19 (2019) 8461–8468.
[68] G. Zhou, M. Lu, Z. Yang, Langmuir 22 (2006) 5900–5903.
[69] D. Mott, J. Galkowski, L. Wang, et al., Langmuir 23 (2007) 5740–5745.
[70] Z. Zhang, S.S. Wang, R. Song, et al., Nat. Commun. 8 (2017) 488.
[71] F.S. Roberts, K.P. Kuhl, A. Nilsson, Angew. Chem. Int. Ed. 54 (2015) 5179–5182.
[72] P. Grosse, D. Gao, F. Scholten, et al., Angew. Chem. Int. Ed. 57 (2018) 6192–6197.
[73] P. Zhu, C. Xia, C.Y. Liu, et al., Proc. Natl. Acad. Sci 118 (2021) e2010868118.
[74] Y. Hori, I. Takahashi, O. Koga, et al., J Phys. Chem. B 106 (2002) 15–17.
[75] A.A. Peterson, F. Abild-Pedersen, F. Studt, et al., Energy Environ. Sci. 3 (2010) 1311–1315.
[76] A.J. Garza, A.T. Bell, M. Head-Gordon, ACS Catal. 8 (2018) 1490–1499.
[77] K. Tran, Z.W. Ulissi, Nat. Catal. 1 (2018) 696–703.
[78] A. Bagger, W. Ju, A.S. Varela, et al., ACS Catal. 9 (2019) 7894–7899.
[79] T.K. Todorova, M.W. Schreiber, M. Fontecave, ACS Catal. 10 (2019) 1754–1768.
[80] H. Xiao, T. Cheng, W.A. Goddard, J. Am. Chem. Soc. 139 (2016) 130–136.
[81] F. Calle-Vallejo, M.T.M. Koper, ACS Catal. 7 (2017) 7346–7351.
[82] X. Nie, W. Luo, M.J. Janik, et al., J. Catal. 312 (2014) 108–122.
[83] X. Nie, M.R. Esopi, M.J. Janik, et al., Angew. Chem. Int. Ed. 52 (2013) 2459–2462.
[84] K. Schouten, E.P. Gallent, M. Koper, J. Electroanal. Chem. 716 (2014) 53–57.
[85] L. Ou, K. Zhao, ACS Omega 4 (2019) 17269–17278.
[86] J.H. Montoya, A.A. Peterson, J.K. Nørskov, ChemCatChem 5 (2013) 737–742.
[87] J.H. Montoya, C. Shi, K. Chan, et al., J. Phys. Chem. Lett. 6 (2015) 2032–2037.
[88] A.A. Peterson, J.K. Nørskov, J. Phys. Chem. Lett. 3 (2012) 251–258.
[89] J. Hussain, H. Jonsson, E. Skulason, ACS Catal. 8 (2018) 5240–5249.
[90] W. Luo, X. Nie, M.J. Janik, et al., ACS Catal. 6 (2016) 219–229.
[91] R.M. Aran-Ais, D. Gao, B.Roldan Cuenya, Acc. Chem. Res. 51 (2018) 2906–2917.
[92] D. Ren, J. Fong, B.S. Yeo, Nat. Commun. 9 (2018) 925.
[93] P. De Luna, R. Quintero-Bermudez, C.T. Dinh, et al., Nat. Catal. 1 (2018) 103–110.
[94] A.S. Varela, M. Kroschel, T. Reier, et al., Catal. Today 260 (2015) 8–13.
[95] Y.F. Bu, M. Zhao, G.X. Zhang, et al., ChemElectroChem 6 (2019) 1831–1837.
[96] H. Xiao, T. Cheng, W.A. Goddard, et al., J. Am. Chem. Soc. 138 (2016) 483–486.
[97] D.W. DeWulf, W. David, J. Electrochem. Soc. 136 (1989) 1686–1691.
[98] R.B. Sandberg, J.H. Montoya, K. Chan, et al., Surf. Sci. 654 (2016) 56–62.
[99] J.D. Goodpaster, A.T. Bell, M. Head-Gordon, et al., J. Phys. Chem. Lett. 7 (2016) 1471–1477.
[100] T. Cheng, H. Xiao, W.A. Goddard, Proc. Natl. Acad. Sci 114 (2017) 1795–1800.
[101] J.E. Pander, D. Ren, Y. Huang, et al., ChemElectroChem 5 (2018) 219–237.
[102] K. Jiang, R.B. Sandberg, A.J. Akey, et al., Nat. Catal. 1 (2018) 111–119.
[103] J.K. Nørskov, J. Rossmeisl, A. Logadottir, et al., J. Phys. Chem. B 108 (2004) 17886–17892.
[104] R. Kortlever, J. Shen, K.J.P. Schouten, et al., J. Phys. Chem. Lett. 6 (2015) 4073–4082.
[105] E. Perez-Gallent, G. Marcandalli, M.C. Figueiredo, et al., J. Am. Chem. Soc. 139 (2017) 16412–16419.
[106] H. Li, Y. Li, M.T. Koper, et al., J. Am. Chem. Soc. 136 (2014) 15694–15701.
[107] F. Calle-Vallejo, M. Koper, Angew. Chem. Int. Ed. 52 (2013) 7282–7285.
[108] X. Liu, P. Schlexer, J. Xiao, et al., Nat. Commun. 10 (2019) 32.
[109] Y.G. Kim, A. Javier, J.H. Baricuatro, et al., J. Electroanal. Chem. 780 (2016) 290–295.
[110] Y.Y. Birdja, M.T.M. Koper, J. Am. Chem. Soc. 139 (2017) 2030–2034.
[111] R.A. Van Santen, Acc. Chem. Res. 42 (2009) 57–66.
[112] R. Huang, Y.H. Wen, Z.Z. Zhu, et al., J. Mater. Chem. 21 (2011) 11578–11584.
[113] B. Lang, Surf. Sci. 53 (1975) 317–329.
[114] W.J. Durand, A. Peterson, F. Studt, et al., Surf. Sci. 605 (2011) 1354–1359.
[115] Z. Zhao, Z. Chen, X. Zhang, et al., J. Phys. Chem. C 120 (2016) 28125–28130.
[116] W. Tang, A.A. Peterson, A.S. Varela, et al., Phys. Chem. Chem. Phys. 14 (2012) 76–81.
[117] X. Liu, J. Xiao, H. Peng, et al., Nat. Commun. 8 (2017) 15438.
[118] C. Shi, H.A. Hansen, A.C. Lausche, et al., Phys. Chem. Chem. Phys. 16 (2014) 4720–4727.
[119] Q. Lu, A.L. Wang, H. Cheng, et al., Small 14 (2018) 1801090.
[120] C.M. Gabardo, C.P. O'Brien, J.P. Edwards, et al., Joule 3 (2019) 2777–2791.
[121] Q. Lu, A.L. Wang, Y. Gong, et al., Nat. Chem. 10 (2018) 456–461.
[122] S. Han, Q. Yun, S. Tu, et al., J. Mater. Chem. A 7 (2019) 24691–24714.
[123] F.P. García, D. Cao-Thang, A. Ozden, et al., Science 367 (2020) 661–666.
[124] A. Murata, Y. Hori, Bulletin. Chemical. Soc. Jpn. 64 (1991) 123–127.
[125] C.G. Morales-Guio, E.R. Cave, S.A. Nitopi, et al., Nat. Catal. 1 (2018) 764–771.
[126] A.L. Wang, L. Zhu, Q. Yun, et al., Small 16 (2020) 2003782.
[127] S. Han, C. He, Q. Yun, et al., Coord. Chem. Rev. 445 (2021) 214085.
[128] Q. Yun, Q. Lu, C. Li, et al., ACS Nano 13 (2019) 14329–14336.